

# Fabrication of chitosan-coated mixed spinel ferrite integrated with graphene oxide (GO) for magnetic extraction of viral RNA for potential detection of SARS-CoV-2

Vijay Singh (✉ [singhvj1793@gmail.com](mailto:singhvj1793@gmail.com))

Himachal Pradesh University <https://orcid.org/0000-0001-6693-6176>

Khalid Mujasam Batoo

King Saud University, <https://orcid.org/0000-0001-8264-8203>

Mahavir Singh

Himachal Pradesh University <https://orcid.org/0000-0002-1778-4855>

---

## Research Article

**Keywords:** Magnetic nanoparticles, Magnetic nanocomposite, SARS-COV-2, COVID-19, spinel ferrite, viral extraction

**Posted Date:** August 23rd, 2021

**DOI:** <https://doi.org/10.21203/rs.3.rs-828045/v1>

**License:** © ⓘ This work is licensed under a Creative Commons Attribution 4.0 International License.

[Read Full License](#)

---

**Version of Record:** A version of this preprint was published at Applied Physics A on November 27th, 2021. See the published version at <https://doi.org/10.1007/s00339-021-05067-7>.

# **Fabrication of chitosan-coated mixed spinel ferrite integrated with graphene oxide (GO) for magnetic extraction of viral RNA for potential detection of SARS-CoV-2**

**Vijay Singh<sup>1\*</sup>, Khalid Mujasam Batoo<sup>2</sup>, Mahavir Singh<sup>1</sup>**

<sup>1</sup>Department of Physics, Himachal Pradesh University, Shimla 171005, India

<sup>2</sup>King Abdullah Institute for Nanotechnology, King Saud University, P.O. Box-2455, Riyadh-11451, Saudi Arabia

## **ORCID iD:**

- Vijay Singh (0000-0001-6693-6176)
- Khalid Mujasam Batoo (0000-0001-8264-82)
- Mahavir Singh (0000-0002-1778-4855)

**\*Author for correspondence:** \*Vijay Singh ([bharmoriavij.93@gmail.com](mailto:bharmoriavij.93@gmail.com))

## **Abstract**

Genetic variants of the COVID-19 causative virus have been arising and circulating globally. In many countries especially in developing ones with a huge population, vaccination has become one of the major challenges. SARS-CoV-2 variants' fast transmission rate has upsurge the COVID cases, leading to more stress on health systems. In the current COVID-19 scenario, there is the requirement of more adequate diagnostic approaches to check the COVID-19 spread. Out of many diagnostic approaches, a magnetic nanoparticle-based reverse transcription-polymerase chain reaction could be nontrivial. The use of magnetic nanoparticles to separate nucleic acid of SARS-CoV-2 from the patient samples and applied for detection is an easy and more effective way for COVID-19 patient detection. Herein, the magnetic nanoparticles are synthesized using the sol-gel autocombustion methods and then, successfully coated with biopolymer (chitosan) using ultra-sonication. Chitosan-coated nanoparticles are successfully integrated into the graphene oxide sheets to introduce carboxyl groups. Crystallite size calculation, morphological and magnetic studies of synthesized magnetic nanoparticles, and multifunctional magnetic nanoparticles are done using XRD, SEM, TEM, and VSM respectively. Besides the potentiality of the fabricated nanocomposites in RNA extraction protocol is also discussed with schematic representation.

**Keywords:** Magnetic nanoparticles, Magnetic nanocomposite, SARS-COV-2, COVID-19, spinel ferrite, viral extraction.

## **Introduction**

Ensuing viral pandemic disease COVID-19 caused by an entirely unique coronavirus (nCoV) "SARS-CoV-2" continues to strike the medical and health sectors [1]. Multiple SARS-COV-2 variants like B.1.1.7, B.1.351, B.1.427, B.1.429, B.1.6172, N450K, and S477N, etc. have worsened the things [1]. These variants can transmit

more easily and quickly, resulting in more COVID-19 cases and potentially more deaths [2]. In countries with huge populations, the shortage of vaccines has become a serious challenge. Besides, the upper possibilities of further SARS-CoV-2 genome mutation are a major challenge within the vaccine or adequate drug development against COVID-19 [3]. Thus aggressive surveillance is required. Early diagnosis of COVID-19 patients is the efficient way to monitor SARS-CoV-2 spread in time and space. Thereby, tracking and mitigating the COVID-19 outbreak. After the successful investigation of SARS-CoV-2 genome sequences, diverse sorts of COVID-19 diagnostic approaches are developed. Out of which reverse transcription-polymerase chain reaction (RT-PCR) is the most sensitive and specific one [4]. Despite the advantages of RT-PCR tests, these tests have limitations like long processing time, high cost, trained operators, and false results, which hinder the potentiality of RT-PCR tests for potential detection and control of the COVID-19 outbreak [5]. These major bottlenecks in conventional detection techniques are often avoided with methodological simplification. Magnetic separation (MS) is an increasingly significant technique for molecular biology. The MS technique is productive for purification at the commercial level [6, 7]. Recently, target-specific magnetic nanocomposites (MNCs) have been developed which in conjugation with an adequate buffer system could make speedy and efficient purification. Centrifugation steps are dodged. Besides, MS protocol provides for facile automation of the entire process and therefore the separation of desired biological entities from the larger sample volumes. MNPs (ferrites) are easy to synthesize, eco-friendly nature, have minimal toxicity, and have unusual physicochemical characteristics [8, 9]. The functionalization of MNPs with biopolymers/synthetic polymers or with graphene and its derivatives (graphene oxide (GO) and reduced graphene oxides (rGO)) increase the prior mentioned characteristics of MNPs [10, 11]. Thus functionalized-MPNs behold the potential to reinforce testing availability and efficiency, thereby benefiting the patient care and COVID-19 infection control. Somvanshi et al. synthesized multifunctional ceramic  $ZnFe_2O_4$  (ZF) to help RNA-extraction protocol for RT-PCR analysis [8]. Bare ZF NPs, synthesized through the sol-gel autocombustion method were stepwise modified with amino ( $-NH_2$ ) and carboxyl ( $-COOH$ ) groups using tetraethyl-orthosilicate (TEOS), (3-aminopropyl)triethoxysilane (APTES), and  $-COOH$  loaded polyvinyl alcohol (PVA). Zhao et al. synthesized multiple  $-COOH$  loaded magnetic composite for MS of SARS-COV-2 RNA through one-step incubation and reported that MS-based protocol is the best technology than usual spin column one [12]. Navas-León D.G. et al. supported Zhao et al. fabrication route has presented a 'simplified three-step method' for gaint production of MNPs for SARS-COV-2 virus RNA separation [4]. Sree Chitra Tirunal Institute for Medical Sciences and Technology (SCTIMST) (India), reported developing an innovative MNPs assisted viral-RNA extraction kit named "Chitra Magna". In this kit, MNPs are used to capture and concentrate the viral-RNA from the COVID patient's sample (DST 2020). Chitosan (CH) and GO are found significant in inhibiting and detecting SARS-CoV-2 [14-17]. CH, a naturally abundant cationic polymer is insoluble in an aqueous medium but soluble in a weakly acidic medium [18]. Majorly consists of  $-NH_2$  and hydroxyl ( $-OH$ ) groups, where  $-NH_2$  group gets converted into soluble  $-NH_3^+$  [19]. This biopolymer, exhibits many meritorious properties likely non-toxicity, biodegradability, biocompatibility, and antimicrobial efficacy. Besides, it has a good chelating effect, especially when solubilize within the weakly ethanoic acid medium [18]. These admirable properties of CH motivated researchers to utilize it against SARS-CoV-2. The study conducted by Gulimiran et al. has revealed the potential of  $\beta$ -CH to strongly bind to the SARS-CoV-2S-Receptor Binding Domain (RBD) [20].

Farzin et al. have fabricated a nanometric gas sensor using CPE-HT18C6(Ag)/chitosan/SiQDs@PAMAM/probe for the voltammetric determination of SARS-CoV-2 RdRP sequence (RdRP\_SARSr-P2) [15]. Thus fabricated sensor possesses a broad linear range of detection, better selectivity, and a low limit of detection (LOD) [15]. Graphene and its derivatives too have a lot to offer against COVID-19, attributing to their unique properties like thermomechanical durability, piezoelectricity, large-surface area, strong antiviral potency, and so on [21, 22]. Graphene derivative GO with the abundance of oxygen-containing –OH, carbonyl (C=O), epoxide, and –COOH functional groups on its basal planes and availability of strong negative surface charge can be used to fabricate better RNA extracted protocol against SARS-COV-2 [17,4]. Among MNPs, ceramics (spinel ferrites, (SFs)) have allured substantial interest attributing to their unusual physicochemical characteristics [23]. Among them, lithium-zinc ferrite (LZFO) is one of the foremost important inverse spinel ferrites owing to its high saturation magnetization, easy preparation, and high adsorption efficacy [10]. About 30% to 40% zinc doping end in a maximum magnetization increase and over this, it starts to decrease [24]. Thus, MNC comprised of LZFO as a magnetic core and biopolymer (CH) - GO matrix could be a greater possibility for SARS-CoV-2 viral extraction protocol. LZFO can be prepared through numerous routes like top-down, bottom-up (chemical synthesis), or biosynthesis [25, 26]. One of the techniques is sol-gel autocombustion (chemical synthesis), an exothermic and self-ignition (low temperature) approach. In this, xerogel was procured from an aqueous sol. having metal salts (oxidizer) and organic complexing agent (reductant) of interest undergoes thermally-induced anionic redox reaction [27]. This low-temperature technique provides; good chemical uniformity (i.e. mingling of metal ions of craved composition at the molecular level); better purity and crystallinity; fine particle size and narrow particle size distribution [28, 29]. Besides, stoichiometry could be comfortably administered, the introduction of dopants into the end product is facile, simple accessories and synthesis process, shorter processing time, low external energy utilization (low-temperature requirement for ignition), and simple operating procedure [28, 30]. Herein, the prime intent is to synthesize diamagnetic Zn<sup>2+</sup> doped lithium ferrite (LF) MNPs for the composition Li<sub>0.33</sub>Zn<sub>0.34</sub>Fe<sub>2.33</sub>O<sub>4</sub> (LZFO) by the sol-gel autocombustion route. Afterward, the prepared nano-sized LZFO particles to be modified with the –NH<sub>2</sub> groups through CH coating. In the end, CHLZFO biocomposite is integrated with GO matrix to introduce carboxyl groups by ultrasonication technique. Later on, synthesized LZFO and MNCs are examined for their structural, morphological, and magnetic characteristics. Besides, how MNC can be used in the magnetic separation of viral-RNA is also discussed (theoretically).

## **Experimental**

### **Materials and Chemicals**

Graphite flakes, hydrazine hydrate, sulphuric acid (H<sub>2</sub>SO<sub>4</sub>), phosphoric acid (H<sub>3</sub>PO<sub>4</sub>), potassium permagnate (KMnO<sub>4</sub>), hydrogen peroxide (H<sub>2</sub>O<sub>2</sub>), Hydrochloric acid (HCL), lithium nitrate (LiNO<sub>3</sub>), zinc nitrate hexahydrate (Zn(NO<sub>3</sub>)<sub>2</sub>.6H<sub>2</sub>O), iron nitrate nonahydrate Fe(NO<sub>3</sub>)<sub>3</sub>.9H<sub>2</sub>O, citric acid (CA) (C<sub>6</sub>H<sub>8</sub>O<sub>7</sub>), ammonia, ethylene glycol (EG), ethanol and chitosan were of analytical grade and used without further purification and treatment. All the chemicals were purchased from central drug house (P) Ltd- CDH Solan, India.

### **Procedures**

### **Synthesis of graphene oxide (GO)**

GO is synthesized by improved hummer method (see **Fig. 1c**: Schematic representation of improved hummer method for **GO** synthesis) [31]. A mixture of sulphuric acid and phosphoric acid ( $H_2SO_4/H_3PO_4$  at a vol. ratio of 9:1 (360:40 mL) was prepared by stirring for 15 min. After, 1.5 g of graphite flakes was added. Next, 18.0 g of  $KMnO_4$  was slowly added into the mixture with continuous stirring. Prepared mixture was for 72 hrs. After 72 hrs of stirring, 3ml of 30 % hydrogen peroxide ( $H_2O_2$ ) was added to end the reaction. Then, the mixture was put into 8 separate 50 ml centrifuge tubes for washing. The washing was done with HCl acid and double distilled water alternately with the centrifugation at 5000 rpm for 10 min for each washing step. Washing steps were repeated thrice. Lastly, the final product was dried in an oven at 80 °C for 24 hours.

### **Synthesis of mixed lithium Zinc ferrite**

Pristine MNPs of LZFO were fabricated by sol-gel combustion method shown in **Fig. 1a**: Schematic representation of sol-gel auto-combustion route for fabrication of **LZFO** [32]. The analytical grade lithium nitrate ( $LiNO_3$ ), zinc nitrate hexahydrate ( $Zn(NO_3)_2 \cdot 6H_2O$ ), iron nitrate nonahydrate  $Fe(NO_3)_3 \cdot 9H_2O$  were used as precursor materials. In stoichiometric amounts these nitrate precursors were dissolved in double distilled water and stirred for 2 hrs to get a homogenous solution. Thereafter, during stirring equimolar citric acid (as fuel) added to the solution which was first separately dissolved in double distilled water. The resulted solution pH was maintained about 7 using ammonia. Then, ethylene glycol ( $C_2H_6O_2$ ) was added to the mixed solution and was heated at 80°C under constant magnetic stirring to get dark colored dried gel. The viscous brown gel followed by foaming of the gel. The foamy gel was at 80°C which caused its spontaneous ignition. The combustion reaction was completed within a few seconds and loose powder was formed. This was crushed and ground thoroughly. The puffy, brown powder as-combusted was calcinated at 500°C for 5 hrs to get pure LZFO.

### **Ultrasonic synthesis of chitosan coated LZFO NPs (CHLZFO nanocomposite)**

CHLZFO nanocomposite was fabricated by Ultra-sonication route (see **Fig. 1b**: Schematic procedure for CHLZFO) [33]. 0.5 g of CH was dissolved in 100 ml of acetic acid (2wt%) solution and 5g amount of LZFO was dispersed in 50ml ethanol by ultrasonication for 2 hrs. Prepared suspension was then, added into the Chitosan solution. Thereafter, the prepared mixture was sonicated for 2 hrs. After that 3ml (25%) glutaraldehyde solution (as a cross-linker) was added and the solution was mechanically stirred for 30 min at 60°C for better crosslink of the chitosan. Then pH about 8 was adjusted by drop wise addition of ammonia solution. The resulted precipitate was separated from the reaction mixture by filtration process, washed several times with double distilled water and dried at 60°C for 10 hrs to obtain the chitosan coated LZFO NPs.

### **Ultra-sonication preparation of CHLZFO-GO nanocomposite**

To prepare CHLZFO-GO nanocomposite, using ultra-sonication method (see **Fig. 1d**: Schematic procedure for CHLZFO-GO nanocomposites) 16:1 ratio of CHLZFO (800 mg) and GO (5 mg) were separately taken in double

distilled water and ultra-sonicated for 1 hr to get uniform dispersion of CHLZFO NPs and colloidal solution of GO. Thereafter, under continuous ultra-sonication, the uniform dispersion of CHLZFO NPs was slowly added to the colloidal solution of GO. Finally, 2ml (25%) glutaraldehyde solution (as cross-linker) was slowly added into the prepared mixture which was then ultra-sonicated for 1hr. In the end, after three washes and simultaneous filtration, the obtained dark greyish red colour precipitate was dried at 50°C for 6 hrs to get the CHLZFO-GO nanocomposite.

### **Characterization**

X-ray diffraction method was employed to authenticate the formation GO, LZFO Mnps, CHLZFO and CHLZFO-GO MNCs. XRD instrument used: PANalytical XPert Pro X-ray diffractometer (India), using  $\text{CuK}\alpha 1$  radiation ( $\lambda = 1.5406 \text{ \AA}$ ) operating at working voltage of 45 kV and working current of 40 mA in  $2\Theta$  range of  $5.070^\circ$  to  $90.010^\circ$  at step size  $0.02^\circ$ . Both the lattice constant and the crystallite size for prepared samples were determined using Debye Scherrer equation. Morphological studies were performed by JEM.2100F Field Emission Electron Microscope and JEOL JSM-7600F Field Emission Scanning Electron Microscope (FESEM) (Saudi Arabia). Furthermore, magnetic characterizes were studied using EV9 Vibrating Sample Magnetometer (EV9 VSM)-MicroSense (India) by applying  $\pm 2$  Tesla field at ambient temperature.

### **Result and Discussion**

#### **LZFO nanopowder by sol-gel auto-combustion**

For sol-gel auto-combustion synthesis of LZFO nanopowder nitrate salts are used as precursors since these are easily soluble in water and can serve as low-temperature  $\text{NO}_3^-$  oxidant source for the preparation process [34]. Metal nitrates are of hygroscopic nature which means they can easily absorb moisture from their surroundings [35]. The selection of a proper complexing agent/fuel agent is significant as it governs the phase formation during the auto-combustion process. Complexing agent agents can serve dual purposes as (i) a fuel for ignition, (where it behaves as a reductant and can get easily oxidized by  $\text{NO}_3^-$  ions), and (ii) a chelating agent to form complex with metal ions [36]. The used complexing agent chelates metal ions by changing ionic radii and prevents their choosy precipitation to keep compositional uniformity among the constituents [36]. The ideal complexing agents should react moderately and generate non-carcinogenic gases [37]. Since hydrazine ( $\text{N}_2\text{H}_4$ ) is carcinogenic it has used seldom as complexant [38]. In the current research,  $\text{C}_6\text{H}_8\text{O}_7$  is used as a complexing agent. CA is the persistently used complexing agent for the synthesis of an ample variety of ferrites through the sol-gel auto-combustion technique. CA significance attributed to the factors: economical, and exhibits  $-\text{COOH}$  groups, and  $-\text{OH}$  groups [36]. Complexing agents having  $-\text{COOH}$  groups,  $-\text{OH}$  groups, and  $-\text{NH}_2$  groups are nontrivial for the water-soluble complex precursor preparation method [36]. The use of complexant in the synthesis procedure governs the temperature and rate of the reaction. Complexant deficiency may lower down the temperature and slows down the rate of reaction due to low heat generation during the reaction which can result in lessening of SFs dimension, poor crystalline nature, and phase purity, and specific area enhancement [38-41]. Thus,  $\text{C}_6\text{H}_8\text{O}_7$  used in the current research is equimolar with metal

nitrate. The addition of CA as a complexant is usually followed by the addition of ammonia (NH<sub>4</sub>OH). In the absence of NH<sub>4</sub>OH, CA will merely act as a fuel. NH<sub>4</sub>OH addition controls oxygen balance (ratio of metal salts to CA), improves the complexation between metal cations and citrates, and enhances the combustion rate of the reaction. This could result in the formation of a porous 3D network structure in the nitrate-citrate gel [42]. The little amount of NH<sub>4</sub>OH added is administered by maintaining solution pH. *Waqas et al.* reported that pH = 6 is the most favorable value for spinel ferrite synthesis [43]. Though, neutral pH (= 7) has been chosen by most of the researchers for the formation of spinel ferrite from the nitrate-citrate xero-gel. In the present research, also pH = 7 is being chosen. C<sub>2</sub>H<sub>6</sub>O<sub>2</sub> is used to terminate the reaction. Its addition to the mixed solution of nitrates and citrates may result in the formation of a single-phase LZFO by decreasing combustion temperature and increasing heat generation in the reaction [44]. In the reaction, EG acts as a gelating reagent and forms an organic ester by forming bonds with citrates [45, 46]. Properties of LZFO nanopowder strongly depend on the heating mechanism used [47, 48]. In this work, a hotplate is used as a heating source. Heating through a hotplate could result in, particles of small and agglomerate sizes with a high area of surface [48]. During the burning of xero-gel gases in large volumes were released, which could have resulted in a great mass loss and led to the formation of brown-colored fluffy LZFO nanopowders [38, 49]. Then the fluffy (porous) LZFO powder was calcinated which formed compact LZFO MNPs (see **Fig. 1a**).

### **X-Ray Diffraction (XRD)**

XRD was used to investigate the crystal phase and to determine the interlayer spacing for GO. **Fig. 2:** shows the XRD spectra for GO, LZFO, CHLZFO, and CHLZFO-GO. For GO, 2 $\theta$  peak can be seen at 9.4563 which confirmed the presence of a well-arranged layer structure with 0.934513 nm d-spacing (FWHM = 0.4655), along with the (002) orientation (**Fig. 2a**) [50]. The XRD patterns shown in **Fig. 2b** depicted the successful fabrication of bare LZFO MNPs, chitosan-coated LZFO NPs, and CHLZFO-GO nanocomposite respectively. For LZFO respective 2 $\theta$  peak values at 18.2780 $^{\circ}$ , 30.1458 $^{\circ}$ , 35.5087 $^{\circ}$ , 37.1763 $^{\circ}$ , 43.1755 $^{\circ}$ , 53.5508 $^{\circ}$ , 57.0963 $^{\circ}$ , and 62.7104 $^{\circ}$  correspond to (111), (220), (311), (222), (400), (222), (400), (422), (511), and (440), crystal planes with no extra peaks were observed [10]. Thus, confirmed the formation of pure single-phase cubic spinel structure of LZFO devoid of impurities. All the diffraction peaks observed herein are in good agreement with those reported in the literature [10]. The diffraction patterns for CHLZFO and CHLZFO-GO NCs found analogous to the diffraction patterns LZFO. Thereby, revealing that no significant variation was observed in the orientation of NPs in the respective nanocomposites. Absence of diffraction peaks of CH and GO in respective XRD patterns of CHLZFO and CHLZFO-GO illustrated the successful coating of chitosan on LZFO NPs and the successful exfoliation of GO to a large extent with successful deposition of CHLZFO NPs on it indicating the formation of nanocomposite [51]. The noise observed in the XRD patterns of CHLZFO and CHLZFO-GO NCs respectively is attributed to the amorphous nature of chitosan.

The values of lattice parameter (a), d-spacing (dhkl), and average crystallite size (<D>) for LZFO, CHLZFO, and CHLZFO-GO were determined from the diffraction peaks with 100% relative intensity correspond to the crystal

plane (311) respectively, using the formulae represented by equation (1), Bragg's law equation (2) and equation (3) (Scherrer's formula) [10].

$$a = \frac{\lambda[h^2+k^2+l^2]^{1/2}}{2 \sin \theta} \quad (1)$$

$$2d_{hkl} \sin \theta = n\lambda \quad (2)$$

$$\langle D \rangle = \frac{K\lambda}{\beta_{hkl} \cos \theta} \quad (3)$$

Where,  $a$  is the lattice parameter,  $d_{hkl}$  is the interplanar spacing,  $\langle D \rangle$  is the average crystallite size,  $\lambda$  ( $= 1.5406 \text{ \AA}$  for Cu-K $\alpha_1$ ) is the X-ray radiation,  $\theta$  is the Bragg angle (scattering angle),  $\beta$  is the full-width half maxima (FWHM), and  $K$  is a constant ( $= 0.94$ ).

The calculated values of crystallite size, lattice constant, d-spacing, and volume are shown in **Table 1**.  $\langle D \rangle$  for CHLZFO-GO, CHLZFO, and LZFO were found in the range of 23 nm to 35 nm. The unit cell parameters of composites of LZFO are found slightly low compared to bare LZFO. These results reveal the presence of a slight strain occurring in composites which distorted the crystal lattice of individual phases to change the lattice parameter confirming the reduction in the size of MNCs, attributed to the high ultrasonication treatment time [52].

### SEM and TEM analysis

The FESEM images of LZFO NPs, CHLZFO nanocomposite, and CHLZFO-GO are given in **Fig. 3**. a, b, and c: FESEM micrographs of LZFO, CHLZFO, and CHLZFO-GO at 100 nm scale respectively, which revealed spherical and irregular shaped nano-sized morphologies. Agglomerations of the crystallites are also observed, which is attributed to synthesis technique [53]. No significant information about functionalization can be made out from FESEM images. HRTEM micrographs of bare LZFO-MNPs, CHLZFO, and CHLZFO-GO nanocomposite showed in **Fig. 3**.d, e, f: (HR-TEM micrographs of LZFO, CHLZFO, and CHLZFO-GO) revealed the existence of some spherical and irregular shaped nanometric structure with an average size of about 38 nm, 26 nm, and 19 nm. **Fig. 3e** showed the HRTEM image of CHLZFO biocomposite which revealed the successful coating of LZFO by biopolymer CH. The micrograph in **Fig. 3f** depicted the successful entrapping of CHLZFO nanostructured particles inside the GO matrix can be observed. Thus, images of HRTEM clearly indicate the successful functionalization of LZFO which confirmed the making of CHLZFO-GO nanocomposites. HRTEM lattice fringe patterns of synthesized bare MNPs, and magnetic nanocomposites in **Fig. 3**. g,h, i: (HRTEM lattice fringe patterns of LZFO, CHLZFO, and CHLZFO-GO) showed a close association of the lattice planes of bare LZFO, CHLZFO, and CHLZFO-GO respectively. These HRTEM micrographs also showed that the prepared samples are of crystalline nature. But composites of LZFO compared to it are lesser crystalline, because of the CH coating and GO matrix [10]. Thus, these micrographs clearly indicate the successful biopolymer coating and incorporation of CHLZFO in the matrix of GO. Crystallite sizes observed in HRTEM analysis are in good agreement with what was calculated from XRD-study.

### Magnetic Hysteresis Parameters study

Magnetic parameters, saturation magnetization ( $M_s$ ), magnetic coercivity ( $H_c$ ), magnetic remanence ( $M_r$ ), and squareness ( $R$ ) of the prepared LZFO NPs, CHLZFO, and CHLZFO-GO nanocomposites are shown in the table. All three samples showed an increase in magnetization value at the low magnetic field ( $B$ ) and achieve saturation for  $B < 10$  kOe, revealing the presence of long-range ferromagnetic ordering (shown in **Fig. 4**: Magnetic hysteresis of LZFO, CHLZFO, and CHLZFO-GO respt.). Maximum saturation magnetization value 67.1955 emu/g was observed for bare LZFO with a lower  $H_c$  value of 94.492 Oe. For CHLZFO nanocomposite and CHLZFO-GO nanocomposite, the observed  $M_s$  values are 21.597 emu/g and 19.330 emu/g to corresponding  $H_c$  values 103.213 Oe and 102.771 Oe respectively. The variation in magnetization of the prepared samples is mainly attributed to the change in the particle size and the presence of amorphous polymer and nonmagnetic matrix [54, 10]. Due to the high surface-to-volume ratio of smaller CHLZFO and CHLZFO-GO NPs, the surface effects like spin disorder and dead layer on the surface arise leading to the decrease in magnetization value [55]. The higher  $M_s$  value of bare LZFO MNPs is attributed to their better crystal structures which are inconsistent with HRTEM and XRD data [56]. Other anticipated theories which describe the obtained higher  $M_s$  value may be superexchange interaction (Metal-Oxygen-Metal),  $Zn^{2+}$  presence on octahedral site, and divergence of Néel's collinear model [24, 57]. The squareness ( $R = M_r/M_s$ ) values between 0 and 1 tell about the magnetic domain structure. For  $M_r/M_s < 1/2$ , the material exhibits a multi-domain structure, while for  $M_r/M_s \geq 1/2$ , the material possesses a single domain structure [58]. Herein, LZFO-MNPs have a high  $M_r/M_s$  value compared to CHLZFO and CHLZFO-GO NCs indicate high magnetocrystalline anisotropy due to its better crystalline nature [59]. Lower  $M_r/M_s$  values for MNCs are attributed to the decrease in crystal order and structure, because of the presence of the amorphous polymer and matrix of GO.  $R$  values for the samples prepared in present work lie from 0.178 to 0.265. Thus, revealing the multi-domain structure for the prepared samples. In literature, ample studies reported an increment in the magnetization of LF on the addition of  $Zn^{2+}$ . Panchel et al. obtained  $M_s = 64.6$  emu/g for LF doped with  $Zn = 0.25$ , synthesized by sol-gel method. Crystallite sizes calculated by Panchel et al. were in the range 27 – 38 nm without calcination [60]. Gee et al. synthesized  $Zn^{2+}$  doped LF for many compositions using the ball milling synthesis route.  $M_s = 80$  emu/g was reported for  $Zn = 0.30$  and average crystallite size value was in the range 20 nm - 50 nm [61]. Mallick et al. synthesized mixed lithium zinc ferrite using  $Zn = 0.38$  by sol-gel route followed by 6 hours calcination at 500<sup>o</sup> C. The average values crystallite size was in the range of 13 – 23 nm and  $M_s$  values reported are 62 and 95.5 emu/g at 300 K and 5 K respectively [10].

### CHLZFO-GO assisted RNA extraction protocol

SARS-CoV-2s' RNA isolated using CHLZFO-GO MNCs can be examined either by standard RT-PCR (eluted product to be used) or Direct RT-PCR (CHLZFO-GO/RNA complex without elution). Extraction protocol comprised of simple steps like lysis/binding buffer combination with CHLZFO-GO NCs in a single step, followed by the throw out of liquid above the formed complex, washing, elution, and finally assembling the extracted RNA for RT-PCR shown in **Fig.5a**: (Schematic representation of CHLZFO-GO MNCs based viral- RNA separation protocol) [8,12]. The CHLZFO-GO/RNA complex can be used directly for RT-PCR reaction without elution. In

direct subjection, all extracted viral-RNA are subjected to amplification which can lessen the cycle threshold value compared to the usual protocol. Therefore, in the direct RT-PCR protocol, the possibility of receiving false-negative results can be further reduced. The prepared MNCs can offer the better binding performance with nucleic acid, thereby improving the sensitivity and linearity of the diagnostic technique. Besides excellent performances, other merits of CHLZFO-GO assisted RNA isolation protocol like fewer operating hours, simplicity, and correct diagnosis (**Fig. 5b**: Merits of Direct RT-PCR). The current viral-extraction protocol can be automated, which will overcome the current issue of centrifugation of conventional technique [8]. The MS of RNA using CHLZFO-GO MNC is underway and will be reported in the near future.

### The basic mechanism of magnetic separation

In MS targeted biological entities (current research; viral-RNA) to be separated from their native environment and then studied in a controlled environment. This is done in two steps: (i) the viral-RNA tagging with MNPs, and (ii) attached viral-RNA with MNPs extracted or by applying force. Briefly, tagging of viral-RNA to MNPs is achieved by preparation a hull of multifunctional MNPs (CHLZFO-GO). For achieving MS: the viral-RNA/CHLZFO-GO complex should be in a fluid. Then fluid will be exposed to a steep magnetic field gradient. Magnetic force is required to overpower the hydrodynamic drag force and buoyancy force of the fluid. The hydrodynamic drag force [62]:

$$F_d = 6\pi\eta R_m \Delta v, \quad (4)$$

Where  $\eta$  is the viscosity of the fluid,  $R_m$  is the radius of the multifunction MNPs,  $\Delta v = v_m - v_w$ , the difference between velocities of entities and fluid. The radius (size) of the MNPs plays a significant role. Monodisperse particles can provide a very uniform reproducibility of MS. The separation of nanoscale MNPs requires the application of high-gradient magnetic separators. The second competing buoyancy force has small effects in the situation and thus can be neglected [62, 63]. Along with buoyancy, other forces like gravitation and interaction between particles are neglected too [63]. The magnitude of the magnetic force;

$$F_m = \mu_o \chi V_m (B_a \cdot \nabla) B_a \quad (5)$$

Where  $\mu_o$  is the magnetic permeability of free space,  $V_m$  is particles' volume,  $\chi$  is magnetic susceptibility, and  $B_a$  is the applied magnetic field. MNP's motion under magnetic field and viscous fluid can be illustrated by using Newton's law [64]:

$$m_p \frac{dv_p}{dt} = \mu_o \chi V_m (B_a \cdot \nabla) B_a - 6\pi\eta R_m \Delta v \quad (6)$$

Out of various separator designs [62], a simple design is used herein, where the tagged MNPs are exposed to a permanent magnet (placed sidewise, see **Fig. 5a**). It is reasonable to use a magnet from the side of the tube holding the sample mixture for aggregating the MNCs about the tube's wall and pouring away the residue. All viral-RNA tagged MNPs get stuck and the remaining fluid will fly out. Then magnet can be removed and collected CHLZFO-

GO/RNA complex can be washed repeatedly with ethanol (prepared washing buffer sol.), frequency of washing can be twice/thrice. Afterward, the purified SARS-CoV-2 virus-RNA can be separated from MNCs by incubating the CHLZFO-GO/RNA complex in buffer sol. and a certain volume of supernatant can be used for RT-PCR reaction [12]. In literature, the studies reported regarding the use of MS protocol for SARS-CoV-2 virus extraction indicate that the magnetically assisted RT-PCR protocol is better than the standard one. Different MNPs and MNCs used for MS protocol for extraction of nucleic acids of SARS-CoV-2 mentioned in Table 3 along with the synthesis route. The research done by Zhao et al. indicates easy, prompt, and efficient detection of SARS-CoV-2s' nucleic acids by poly-NH<sub>2</sub>-MNP (pcMNPs). pcMNPs assisted MS protocol, is both manual and automated, pcMNPs/RNA complex could be transmitted directly for RT-PCR reaction. Reported extraction time for different samples was approximately 30 min compared to the 2 hr time of the conventional one [12]. Somvanshi et al. showed low-temperature preparation of zinc ferrite whose surface was modified with –NH<sub>2</sub> and –COOH functional groups. Estimated viral-extraction time reported approx. 15 min [8]. Both Somvanshi et al. and Zhao et al. used TEOS to cover the pristine MNPs with silica, and then use APTES and multi-charged polymer -COOH to introduce -NH<sub>2</sub> and –COOH groups. Navas-León D.G. et al. improvised the synthesis technique adopted by Zhao et al. to produce MNPs and MNCs by directly modifying the MNPs' surface with APTES [4]. The possible reason for the formation of the MNCs/SARS-CoV-2-RNA complex reported is the interaction or binding between –NH<sub>2</sub> and –COOH groups with nucleic acids of viral-RNA.

## Conclusion

The multifunctional CHLZFO-GO MNC was successfully synthesized using sol-gel autocombustion and ultrasonication. The nanocrystalline nature, spherical shape, irregularly shaped and functionalization of the bare MNPs, and formation of were authenticated through XRD-patterns, FESEM, and HRTEM images. Crystallite sizes for the synthesized MNPs and nanocomposites were found in the nano-metric range (~ 22 nm to 38 nm). Investigation of magnetic parameters like nature of hysteresis loop,  $M_s$ ,  $H_c$ , and squareness factor confirmed soft magnetic character, decrement in  $M_s$  values LZFO, CHLZFO, and CHLZFO-GO from 67.1955 emu/g, 21.597 emu/g, and 19.330 emu/g verifying size decrement, successful CH coating, and GO integration. The observed magnetization values are suitable for the efficient and robust RNA extraction procedure for the potential detection of SARS-CoV-2 in COVID-19 patients. The MNC assisted RT-PCR technique is simple, economical, time-saving, and much effective in detection, and thus can be seen as a potential substitute for conventional RT-PCR techniques. To employ this protocol for a clinical purposes need more studies. MNC-based extraction can be an innovative technology for isolating RNA from swabs for fast COVID 19 tests at a larger scale.

## References

- [1] [https://www.who.int/en/activities/tracking-SARS-CoV-2-variants/\(2021\)](https://www.who.int/en/activities/tracking-SARS-CoV-2-variants/(2021))
- [2] Bandy, D.J.D.R., Weimer, B.C. (2021) Analysis of SARS-CoV-2 genomic epidemiology reveals disease transmission coupled to variant emergence and allelic variation. *Sci Rep* 11, 7380. <https://doi.org/10.1038/s41598-021-86265-4>

- [3] Lianlian Bian, Fan Gao, Jialu Zhang, Qian He, Qunying Mao, Miao Xu & Zhenglun Liang (2021): Effects of SARS-CoV-2 variants on vaccine efficacy and response strategies, *Expert Rev. Vaccines*, <https://doi.org/10.1080/14760584.2021.1903879>
- [4] Chacón-Torres, J.C., Reinoso, C., Navas-León, D.G. et al. (2020). Optimized and scalable synthesis of magnetic nanoparticles for RNA extraction in response to developing countries' needs in the detection and control of SARS-CoV-2. *Sci Rep* 10, 19004, <https://doi.org/10.1038/s41598-020-75798-9>
- [5] Adeel Afzal, (2020). Molecular diagnostic technologies for COVID-19: Limitations and challenges; *J Adv Res.* 26: 149–159; <https://doi.org/10.1016/j.jare.2020.08.002>
- [6] Safarikova M, Safarik I, (2001) The Application of Magnetic Techniques in Biosciences *Magn. Elect. Separation* 10(4) <https://doi.org/10.1155/2001/57434>
- [7] Franzreb M, Siemann-Herzberg M, Hobley TJ, Thomas ORT (2006) Protein purification using magnetic adsorbent particles. *Appl Microbiol Biotechnol* 70:505–516. <https://doi.org/10.1007/s00253-006-0344-3>
- [8] Sandeep B. Somvanshi S et al. (2020) Multifunctional nano-magnetic particles assisted viral RNA-extraction protocol for potential detection of COVID-19; *Mater. Res. Innov.* 25(3):1-6, <https://doi.org/10.1080/14328917.2020.1769350>
- [9] Islam A, Ahsan Md Z, (2020) Plausible Approach for Rapid Detection of SARS-CoV-2 Virus by Magnetic Nanoparticle Based Biosensors *Md. J. Nanosci. Nanotechnol* 6(2): 6-13 <https://doi.org/10.11648/j.aj.n.20200602.11>
- [10] Mallick, A. S. Mahapatra, A. Mitra, J. M. Greneche, R. S. Ningthoujam, P. K. Chakrabarti; (2018). Magnetic properties and bio-medical applications in hyperthermia of lithium zinc ferrite nanoparticles integrated with reduced graphene oxide, *J. Appl. Phys.* 123, 055103; <https://doi.org/10.1063/1.5009823>
- [11] Teresa Lage, Raquel O. Rodrigues, Susana Catarino, Juan Gallo, Manuel Bañobre-López, Graça Minas, (2021) Graphene-Based Magnetic Nanoparticles for Theranostics: An Overview for Their Potential in Clinical Application *Nanomaterials*, 11, 1073. <https://doi.org/10.3390/nano11051073>
- [12] Zhao Z, Cui H, Song W, Ru X, Zhou W, Yu X; (2020) A simple magnetic nanoparticles-based viral RNA extraction method for efficient detection of SARS-CoV-2. *bioRxiv* preprint. <https://doi.org/10.1101/2020.02.22.961268>
- [13] <https://dst.gov.in/sree-chitra-tirunal-institute-develops-magnetic-nanoparticle-based-rna-extraction-kit-pcr-and-lamp> (2021).
- [14] Milewska A, Chi Y, Szczepanski A, Duran et al. (2021) HTCC as a Polymeric Inhibitor of SARS-CoV-2 and MERS-CoV, *J. Virol.* 95 (4), e01622-20. <https://doi.org/10.1128/JVI.01622-20>
- [15] Farzin, L., Sadjadi, S., Sheini, A. et al. (2021). A nanoscale genosensor for early detection of COVID-19 by voltammetric determination of RNA-dependent RNA polymerase (RdRP) sequence of SARS-CoV-2 virus. *Microchim Acta* 188, 121. <https://doi.org/10.1007/s00604-021-04773-6>

- [16] Hathout M R. and Kassem H D., (2020) Positively Charged Electroceutical Spun Chitosan Nanofibers Can Protect Health Care Providers From COVID-19 Infection: An Opinion; *Front Bioeng Biotechnol.*; 8: 885. <https://doi.org/10.3389/fbioe.2020.00885>
- [17] Unal, A.M. et al. (2021) Graphene Oxide Nanosheets Interact and Interfere with SARS-CoV-2 Surface Proteins and Cell Receptors to Inhibit Infectivity. *Small*, 2101483, 1-13. <https://doi.org/10.1002/sml.202101483>
- [18] Ali A, and Ahmed S., (2017) A review on chitosan and its nanocomposites in drug delivery, *International Journal of Biological Macromolecules*; 109, 273–286, <https://doi.org/10.1016/j.ijbiomac.2017.12.078> 0141-8130
- [19] Madera-Santana TJ, Herrera-Méndez CH, Rodríguez-Núñez JR (2018) An overview of the chemical modifications of chitosan and their advantages. *Green Mater.* 6(4): 131–142, <https://doi.org/10.1680/jgrma.18.00053>
- [20] Gulimiran Alitongbieke, Xiu-min Li, Qi-Ci Wu, Zhi-Chao Lin, Jia-Fu Huang, Yu Xue, Jing-Na Liu, Jin-Mei Lin, Tao Pan, Yi-Xuan Chen, Yi Su, Guo-Guang Zhang, Bo Leng, Shu-Wen Liu, Yu-Tian Pan (2020) Effect of  $\beta$ -chitosan on the binding interaction between SARS-CoV-2 S-RBD and ACE. <https://doi.org/10.1101/2020.07.31.229781>
- [21] Ievgen S. Donskyi, Chuanxiong Nie, Kai Ludwig, Jakob Trimpert, Rameez Ahmed, Elisa Quaaas, Katharina Achazi, Jörg Radnik, Mohsen Adeli, Rainer Haag, Klaus Osterrieder, (2021), SARS-CoV-2 Inhibitors: Graphene Sheets with Defined Dual Functionalities for the Strong SARS-CoV-2 Interactions, *Small*. Vol.17, (11), 2170046, <https://doi.org/10.1002/sml.202170046>
- [22] Kumar Raghav , P, Mohanty S. (2020) Are graphene and graphene-derived products capable of preventing COVID-19 infection? *Med. Hypotheses*. 144:110031. <https://doi.org/10.1016/j.mehy.2020.110031>
- [23] Amiri M, Niasari M S, and Akbari A, (2019) Magnetic nanocarriers: Evolution of spinel ferrites for medical applications, *J. Colloid Interface Sci.* 265(2), <https://doi.org/10.1016/j.cis.2019.01.003>
- [24] Kishan, P., Sagar, D.R., Chatterjee, S.N. et al. (1984). Curie temperatures and  $0^\circ\text{K}$  magnetic moments of zinc-substituted lithium ferrites. *Bull. Mater. Sci.* 6, 39–45, <https://doi.org/10.1007/BF02744167>
- [25] Leena Mohammed, Hassan G. Goma, Doaa Ragab, Jesse Zhu, (2016) Magnetic nanoparticles for environmental and biomedical applications: A review, *J. partic.* 921, 1-14, <https://doi.org/10.1016/j.partic.2016.06.001>
- [26] Valenzuela R, (2012) Novel applications of ferrites; *Phys. Res. Int.* vol. 2012, 9, <https://doi.org/10.1155/2012/591839>
- [27] Airimioaei M, Ciomaga C E, Apostolescu N, et al. (2011) Synthesis and functional properties of the  $\text{Ni}_{1-x}\text{Mn}_x\text{Fe}_2\text{O}_4$  ferrites. *J. Alloys Compd.* 509(31): 8065–8072. [10.1016/j.jallcom.2011.05.034](https://doi.org/10.1016/j.jallcom.2011.05.034)
- [28] Costa A C F M, Morelli M R, Kiminami R H G A. (2007) Microstructure and magnetic properties of  $\text{Ni}_{1-x}\text{Zn}_x\text{Fe}_2\text{O}_4$  synthesized by combustion reaction. *J. Mater. Sci.* 42(3): 779–783.
- [29] George M, Mary John A, Nair S S, et al. (2006) Finite size effects on the structural and magnetic properties of sol-gel synthesized  $\text{NiFe}_2\text{O}_4$  powders. *J. Magn. Mater.* 302(1): 190–195. <http://dx.doi.org/10.1016/j.jmmm.2005.08.029>

- [30] Mukasyan A S, Epstein P, Dinka P. (2007) Solution combustion synthesis of nanomaterials. *P. Combust. Inst.* 31(2): 1789–1795. [10.1016/j.proci.2006.07.052](https://doi.org/10.1016/j.proci.2006.07.052)
- [31] Marcano DC, Kosynkin DV, Berlin JM, Sinitskii A, Sun Z, Slesarev A, Alemany LB, Lu W, Tour JM. Improved synthesis of graphene oxide. *ACS Nano.* 2010 Aug 24;4(8):4806-14. <https://doi.org/10.1021/nn1006368>
- [32] Jasrotia R, Virender, Singh P, Kumar R, Singh M, (2019) Raman spectra of sol-gel auto-combustion synthesized Mg-Ag-Mn and Ba-Nd-Cd-In ferrite based nanomaterials, *Ceram. Int.* 46(1), <https://doi.org/10.1016/j.ceramint.2019.09.012>
- [33] Kiran, Kumar S, Thakur N, (2018) Structural and Electrical Properties of Chitosan - Spinel  $MnFe_2O_4$  Biocomposites, *AIP Conf. Proc.* 2220, 020182-1–020182-6. <https://doi.org/10.1063/5.0002383>
- [34] Selvan R K, Augustin C O, Berchmans L J, Saraswathi R, (2003) Combustion synthesis of  $CuFe_2O_4$ . *Mater. Res. Bull.* 38(1): 41–54, [https://doi.org/10.1016/S0025-5408\(02\)01004-8](https://doi.org/10.1016/S0025-5408(02)01004-8)
- [35] Mangalaraja R V, Ananthakmar S, Manohar P, et al. (2004) Characterization of  $Mn_{0.8}Zn_{0.2}Fe_2O_4$  synthesized by flash combustion technique. *Mater. Sci. Eng. A*, 367(1–2): 301–305. <https://doi.org/10.1016/j.msea.2003.10.283>
- [36] Wu K H, Ting T H, Li M C, et al. (2006) Sol–gel auto-combustion synthesis of  $SiO_2$ -doped NiZn ferrite by using various fuels. *J. Magn. Magn. Mater.* 298(1): 25–32. <https://doi.org/10.1016/j.jmmm.2005.03.008>
- [37] Patil J Y, Khandekar M S, Mulla I S, et al. (2012) Combustion synthesis of magnesium ferrite as liquid petroleum gas (LPG) sensor: Effect of sintering temperature. *Curr. Appl. Phys.* 12(1): 319–324. <https://doi.org/10.1016/j.cap.2011.06.029>
- [38] Sertkol M, Kõseoglu Y, Baykal A, et al. (2009) Synthesis and magnetic characterization of  $Zn_{0.7}Ni_{0.3}Fe_2O_4$  nano particles via microwaveassisted combustion route. *J. Magn. Magn. Mater.* 322(7): 866–871, <https://doi.org/10.1016/j.jmmm.2009.11.018>
- [39] Costa A C F M, Morelli M R, Kiminami R H G A. (2001) Combustion synthesis: Effect of urea on the reaction and characteristics of Ni–Zn ferrite powders. *J. Mater. Synthesis Processing*, 9(6): 347–352.
- [40] Verma S, Karande J, Patidar A, et al. (2005) Low-temperature synthesis of nanocrystalline powders of lithium ferrite by an autocombustion method using citric acid and glycine. *Mater. Lett.* 59 (21): 2630–2633. <https://doi.org/10.1016/j.matlet.2005.04.005>
- [41] Xue H, Li Z, Wang X, et al. (2007) Facile synthesis of nanocrystalline zinc ferrite via self-propagating combustion method. *Mater. Lett.* 61(2): 347–350.
- [42] Yue Z, Guo W, Zhou J, et al. (2004) Synthesis of nanocrystalline ferrites by sol–gel combustion process: the influence of pH value of solution. *J. Magn. Magn. Mater.* 270(1–2): 216–223. <https://doi.org/10.1016/j.jmmm.2003.08.025>
- [43] Waqas H, Qureshi A H. (2009) Influence of pH on nanosized Mn–Zn ferrite synthesized by sol–gel auto combustion process. *J. Therm. Anal. Calorim.* 98(2): 355–360. <https://doi.org/10.1007/s10973-009-0289-8>

- [44] Vivekanandhan S, Venkateswarlu M, Satyanarayana N. (2004) Effect of ethylene glycol on polyacrylic acid based combustion process for the synthesis of nano-crystalline nickel ferrite ( $\text{NiFe}_2\text{O}_4$ ). *Mater. Lett.* 58(22–23): 2717–2720. <https://doi.org/10.1016/j.matlet.2004.02.030>
- [45] Kadu A V, Jagtap S V, Chaudhari G N. Studies on the preparation and ethanol gas sensing properties of spinel  $\text{Zn}_{0.6}\text{Mn}_{0.4}\text{Fe}_2\text{O}_4$  nanomaterials. *Current Applied Physics*, 2009, 9(6): 1246–1251. <https://doi.org/10.1016/j.cap.2009.02.001>
- [46] Vijaya Bhasker Reddy P, Ramesh B, Gopal Reddy C. (2010) Electrical conductivity and dielectric properties of zinc substituted lithium ferrites prepared by sol–gel method. *Physica B: Condens. Matter.* 405(7): 1852–185. <https://doi.org/10.1016/j.physb.2010.01.062>
- [47] Costa A C F M, Vieira D A, Silva V J, et al. (2009) Synthesis of the Ni– Zn–Sm ferrites using microwaves energy. *J. Alloy Compd.* 483(1–2): 37–39. [10.1016/j.jallcom.2008.08.096](https://doi.org/10.1016/j.jallcom.2008.08.096)
- [48] Costa A C F M, Tortella E, Morelli M R, et al. (2002) Effect of heating conditions during combustion synthesis on the characteristics of  $\text{Ni}_{0.5}\text{Zn}_{0.5}\text{Fe}_2\text{O}_4$  nanopowders. *J. Mater. Sci.* 37(17): 3569–3572. <https://doi.org/10.1023/A:1016528302082>
- [49] Yu L, Cao S, Liu Y, et al. (2006) Thermal and structural analysis on the nanocrystalline NiCuZn ferrite synthesis in different atmospheres. *J. Magn. Mater.* 301(1): 100– 106. <https://doi.org/10.1016/j.jmmm.2005.06.020>
- [50] Hidayah N. M. S., Liu Wei-Wen, Lai Chin-Wei, Noriman N. Z., Khe C. S. et al., (2017) Comparison on graphite, graphene oxide and reduced graphene oxide: Synthesis and characterization. *AIP Conference Proceedings* 1892, 150002; <https://doi.org/10.1063/1.5005764>
- [51] Bhattacharyya, R., Prakash, O., Roy, S. et al. (2019). Graphene oxide-ferrite hybrid framework as enhanced broadband absorption in gigahertz frequencies. *Sci Rep* 9, 12111. <https://doi.org/10.1038/s41598-019-48487-5>
- [52] Sompech S., Srion A., Nuntiya A., (2012) The Effect of Ultrasonic Treatment on the Particle Size and Specific Surface Area of  $\text{LaCoO}_3$ , *Procedia Eng.* 32:1012-1018. <https://doi.org/10.1016/j.proeng.2012.02.047>
- [53] Sukta A. and Mezinskas G., Sol–gel auto-combustion synthesis of spinel-type ferrite nanomaterials, *Front. Mater. Sci.* 2012, 6(2): 128–141, <https://doi.org/10.1007/s11706-012-0167-3>
- [54] Li, Q., Kartikowati, C.W., Horie, S. et al. (2017). Correlation between particle size/domain structure and magnetic properties of highly crystalline  $\text{Fe}_3\text{O}_4$  nanoparticles. *Sci Rep* 7, 9894, <https://doi.org/10.1038/s41598-017-09897-5>
- [55] Kodama R. H., Berkowitz A. E., McNiff E. J. S. Foner (1997) Surface spin disorder in ferrite nanoparticles. *J. Appl. Phys.* 81, 5552; <https://doi.org/10.1063/1.364659>
- [56] Cao, D., Li, H., Pan, L. et al. (2016). High saturation magnetization of  $\gamma\text{-Fe}_2\text{O}_3$  nano-particles by a facile one-step synthesis approach. *Sci Rep* 6, 32360, <https://doi.org/10.1038/srep32360>
- [57] Dormann J. L., Nogues M (1990) Magnetic structures in substituted ferrites, *J. Phys.: Condens. Matter* 2 1223, <https://doi.org/10.1088/0953-8984/2/5/014>

- [58] Dagar S, Hooda A, Khasa S, Malik M, (2019). Rietveld refinement, dielectric and magnetic properties of NBT-Spinel ferrite composites, *J. Alloys Compd.* 806, 737–752, <https://doi.org/10.1016/j.jallcom.2019.07.178>
- [59] Praveena K., and Varma K.B.R., (2014) Improved magneto-electric response in  $\text{Na}_{0.5}\text{Bi}_{0.5}\text{TiO}_3\text{-MnFe}_2\text{O}_4$  composites, *J. Mater. Sci. Mater. Electron.* 25, 111–116. <https://doi.org/10.1007/s10854-013-1557-8>.
- [60] Panchel S., Raghuvanshi S., Gehlot K., Mazaleyrat F., Kane S. N., (2016). Cationic distribution assisted tuning of magnetic properties of  $\text{Li}_{0.5-x/2}\text{Zn}_x\text{Fe}_{2.5-x/2}\text{O}_4$ , *AIP Adv.* 6, 055930, <https://doi.org/10.1063/1.4944517>
- [61] Gee S. H., Hong Y. K., Park M. H., Erickson D. W., Lamb P. J., Sur J., (2002). Synthesis of nanosized  $(\text{Li}_{0.5x}\text{Fe}_{0.5x}\text{Zn}_{1-x})\text{Fe}_2\text{O}_4$  particles and magnetic properties, *J. Appl. Phys.* 91, 7586, <https://doi.org/10.1063/1.1453931>
- [62] Benz M. (2012) *Superparamagnetism: Theory and Applications*, 1-26.
- [63] Harvey, W.T., Carabelli, A.M., Jackson, B. et al. (2021). SARS-CoV-2 variants, spike mutations and immune escape. *Nat Rev Microbiol* 19, 409–42. 4. <https://doi.org/10.1038/s41579-021-00573-02>
- [64] Weizhong Wei, Zhen Wang, (2018) Investigation of Magnetic Nanoparticle Motion under a Gradient Magnetic Field by an Electromagnet. *J. Nanomater.* vol 2018, 5 <https://doi.org/10.1155/2018/6246917>

# Figures

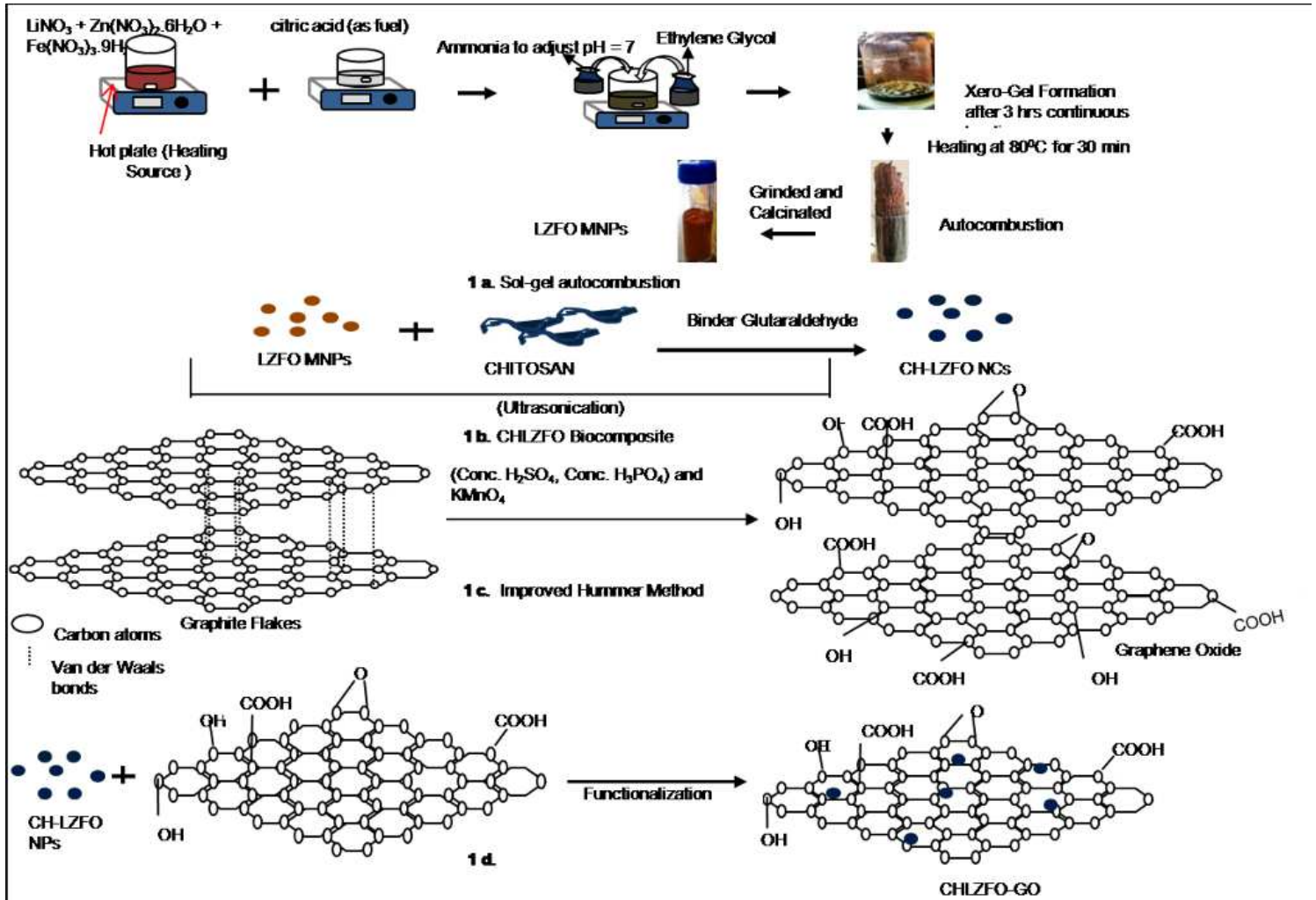


Figure 1

Schematics of synthesis LZFO MNPs, and LZFO nanocomposites

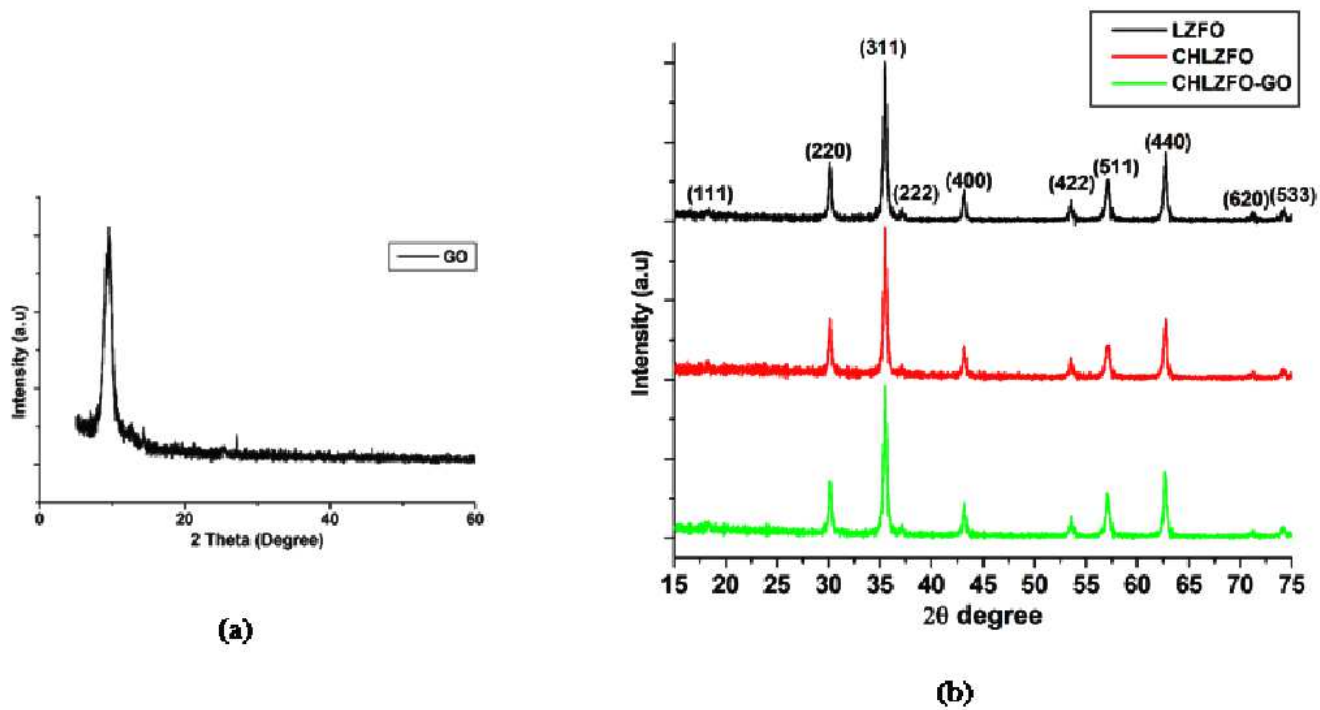
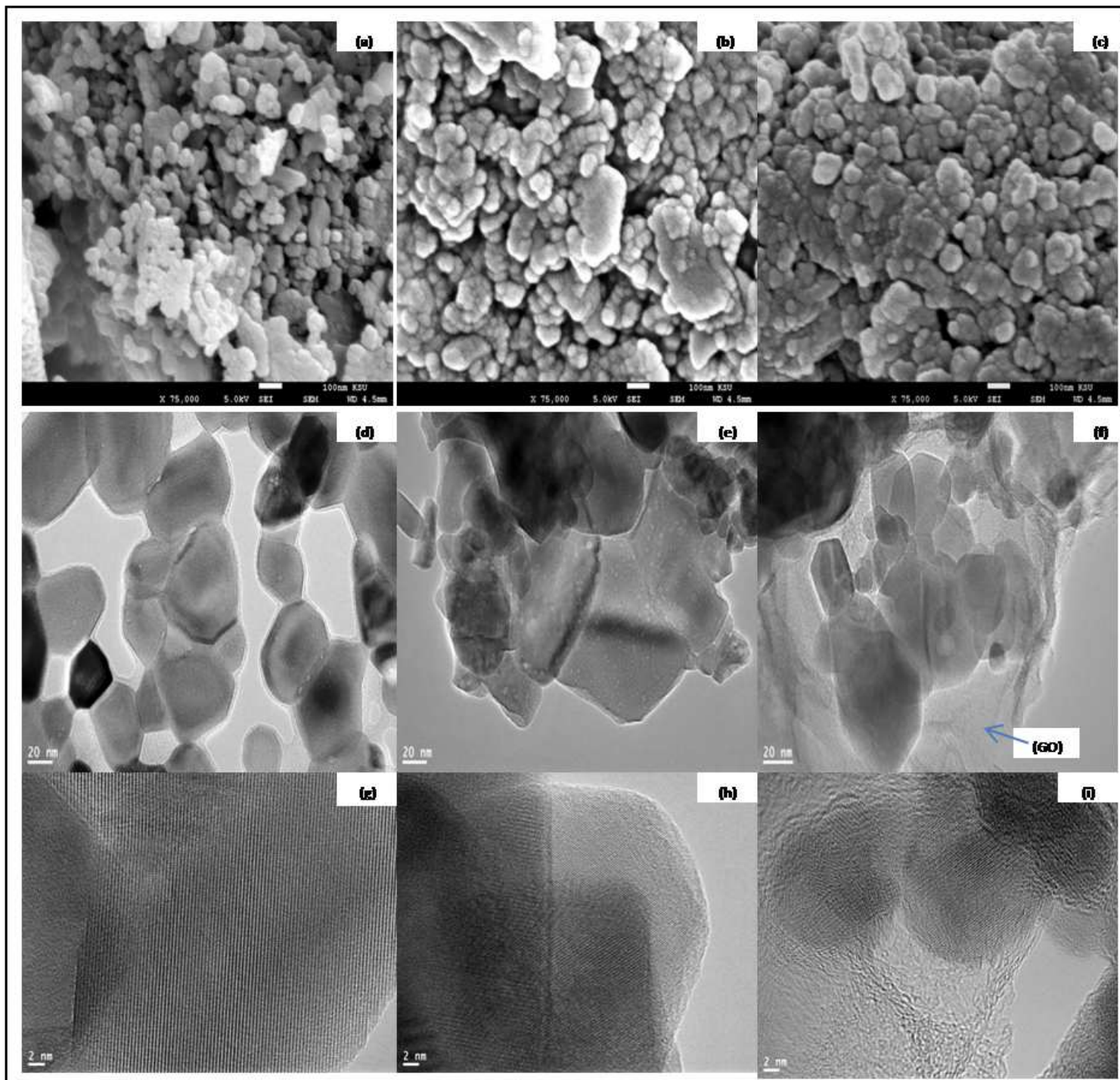


Figure 2

XRD patterns of LZFO, CHLZFO. and CHLZFO-GO



**Figure 3**

FESEM and HRTEM micrographs of LZFO, CHLZFO, and CHLZFO-GO

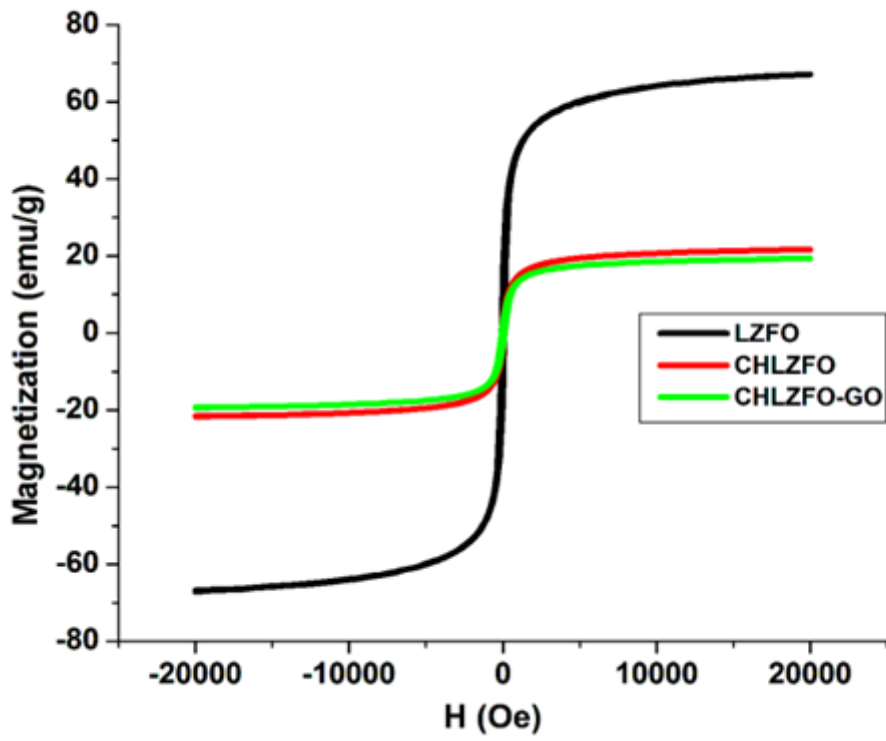


Figure 4

Magnetic hysteresis of pristine LZFO MNPs, CHLZFO, and CHLZFO nanocomposites

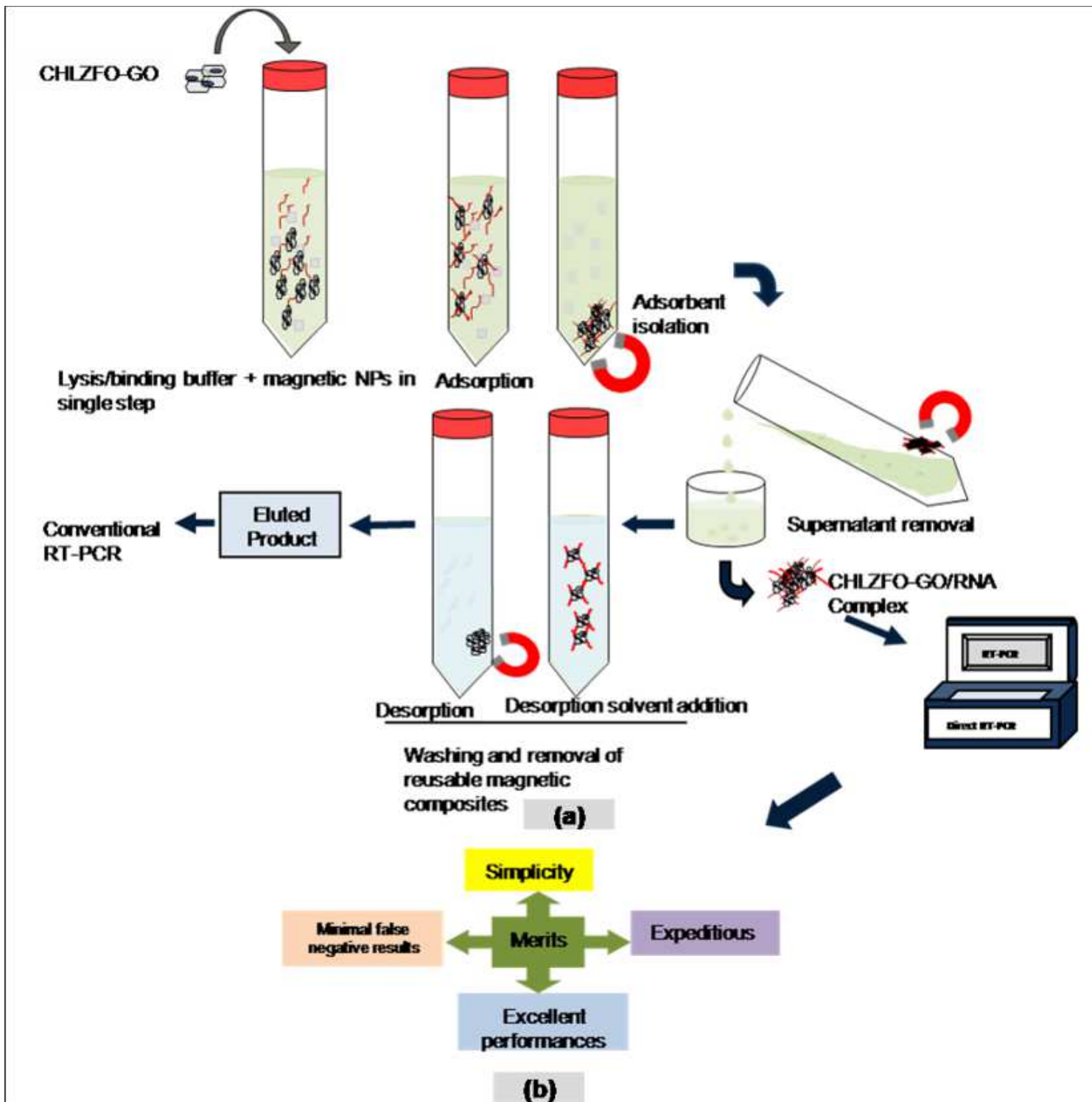


Figure 5

Schematics of RNA extraction using CHLZFO-GO nanocomposites